

A Numerical Algorithm for MHD of Ablated Materials

Tianshi Lu¹, Jian Du², and Roman Samulyak¹

¹Computational Science Center, Brookhaven National Laboratory, Upton, NY 11973, USA

²Department of Applied Mathematics and Statistics, Stony Brook University, Stony Brook, NY 11794, USA

A numerical algorithm for the simulation of magnetohydrodynamics in partially ionized ablated material is described. For the hydro part, the hyperbolic conservation laws with electromagnetic terms is solved using techniques developed for free surface flows; for the electromagnetic part, the electrostatic approximation is applied and an elliptic equation for electric potential is solved. The algorithm has been implemented in the frame of front tracking, which explicitly tracks geometrically complex evolving interfaces. An elliptic solver based on the embedded boundary method were implemented for both two- and three-dimensional simulations. A surface model on the interface between the solid target and the ablated vapor has also been developed as well as a numerical model for the equation of state which accounts for atomic processes in the ablated material. The code has been applied to simulations of the pellet ablation in a magnetically confined plasma and the laser-ablated plasma plume expansion in magnetic fields.

Keywords:

1. INTRODUCTION

Partially ionized ablated materials occur in a variety of applications. Some examples include the ablation of deuterium/tritium pellets injected into the magnetically confined plasma (tokamak) to the expansion of laser generated plasma plumes in nanotube synthesis. Magnetic fields present or introduced in such applications strongly affect the ablation process. The flow of the ablated material is directed along the magnetic field lines and confined in the transverse direction.¹ The ablation rate can also be influenced by the magnetic field.² The simulation of the magnetohydrodynamics (MHD) in partially ionized ablated material presents a new challenge in both the modeling and the numerical algorithm associated with the existence of free surfaces and/or large gradients of flow properties, complex equation of state models, and models for the interaction of plasmas with external sources.²⁻⁴

Weakly ionized plasmas are present in tokamak fueling devices,^{2,3,15} laser ablation in magnetic fields,¹ and other processes in laboratories and in nature.⁵ The major research effort on computational MHD has been in the area of highly ionized plasmas. Numerical algorithms for MHD of partially ionized ablated material have not been sufficiently developed despite the need for fusion research and industrial technologies.

The expanding boundary of the ablated material creates major complications for numerical algorithms. The majority of numerical studies of free surface MHD flows are based on semi-analytical treatment of simplified flow regimes. To the best of our knowledge, the only fully numerical treatment of general free surface incompressible liquid flows is implemented in the HIMAG code⁶ using the level set algorithm for fluid interfaces, the electric potential formulation for electromagnetic forces, and the incompressible fluid flow approximation. In this work, we adapt the numerical algorithm for free surface compressible MHD in the low magnetic Reynolds number approximation¹⁷ to the simulation of weakly ionized plasmas and, in particular, materials ablated by laser pulses of moderate intensities. We would like to note that the low magnetic Reynolds number approximation is not applicable to the simulation of the ablation at high laser intensities (or at least to the period of the initial evolution of the ablated plume) typical for inertially confined fusion experiments.¹ The other important area of application of the proposed numerical method is the simulation of tokamak fueling through the ablation of small frozen deuterium-tritium pellets.⁷ The applicability of the low magnetic Reynolds number approximation to tokamak fueling was shown in Ref. [2].

The key feature of the algorithm is the use of the method of front tracking⁸ for the propagation of vapor interfaces. Our *FronTier* code is capable of tracking and resolving topological changes of large numbers of interfaces

* Author to whom correspondence should be addressed.

in two and three dimensional spaces.⁹ In the method of front tracking, the interface is a Lagrangian mesh moving through a volume filling rectangular mesh according to the solution of the corresponding Riemann problem. High resolution shock capturing Godunov-type solvers are used to update hyperbolic states in the interior away from interfaces. The explicit treatment of interfaces typical for the method of front tracking is especially advantageous for multiphysics problems involving phase transitions. It allows not only to solve accurately the Riemann problem for the phase boundary, but also to apply different mathematical approximations in the regions separated by interfaces to account for different material properties and, if necessary, eliminate fast time scales in numerical simulations. In ablation problems, interfaces between the ablated vapor, the solid target and the ambient gas/plasma are explicitly tracked.

For the study of the MHD effect in ablated material, we exploited the typically low magnetic Reynolds number $Re^M = 4\pi\nu\sigma L/c^2$ in weakly ionized plasmas. This means that the magnetic field is only slightly changed by the induced current, which we will verify *a posteriori*. Under the low magnetic Reynolds number assumption, the evolution of the magnetic field via Faraday's law is not needed. As a result, the electrostatic approximation is valid, and the full MHD system is reduced to the system of hyperbolic conservation laws coupled to an elliptic equation for the electric potential. From computational point of view, such an approach is also beneficial because it effectively removes fast time scales associated with the magnetic field diffusion. The embedded boundary method¹⁰ is used for solving the elliptic problem in geometrically complex domains bounded by vapor interfaces. Proper EOS and conductivity models are applied to the partially ionized ablated material to account for the atomic processes. For the tokamak pellet ablation, a surface ablation model is used at the ablation surface to model the solid-vapor phase transition.²

MHD effect is also important for the control of laser-produced plasma plumes by magnetic fields. Applying magnetic fields to a laser created plumes has been proposed for a better control of the dynamic properties of these transient and energetic plasmas.¹ Simulating the plume expansion using our *FronTier* code equipped with the elliptic solver, we observed the changes in plume structure and dynamics in the presence of the magnetic field.

The paper is organized as follows. In Section 2, we introduce the system of governing equations and discuss mathematical approximations. The numerical algorithm, its implementation in the *FronTier* code, and validation are described in Section 3. Applications of the *FronTier*-MHD code to the numerical simulation of the pellet ablation in a magnetically confined plasma and the expansion of a laser-produced plasma in a magnetic field are presented in Section 4. Finally, we conclude the paper with a summary of our results and perspectives for future work.

2. GOVERNING EQUATIONS

2.1. One Fluid MHD in the Low Magnetic Reynolds Number Approximation

Under the low magnetic Reynolds number approximation,¹² the system of MHD equations for compressible inviscid fluid is the hyperbolic conservation laws of mass, momentum and energy coupled to an elliptic equation for the electric potential. The equations written in Gaussian units are

$$\frac{\partial \rho}{\partial t} = -\nabla \cdot (\rho \mathbf{u}) \quad (1)$$

$$\rho \left(\frac{\partial}{\partial t} + \mathbf{u} \cdot \nabla \right) \mathbf{u} = -\nabla P + \frac{1}{c} (\mathbf{J} \times \mathbf{B}) \quad (2)$$

$$\rho \left(\frac{\partial}{\partial t} + \mathbf{u} \cdot \nabla \right) e = -P \nabla \cdot \mathbf{u} + \frac{1}{\sigma} \mathbf{J}^2 - \nabla \cdot \mathbf{q} \quad (3)$$

$$P = P(\rho, e) \quad (4)$$

$$\mathbf{J} = \sigma \left(-\nabla \varphi + \frac{1}{c} \mathbf{u} \times \mathbf{B} \right) \quad (5)$$

$$\nabla \cdot (\sigma \nabla \varphi) = \frac{1}{c} \nabla \cdot \sigma (\mathbf{u} \times \mathbf{B}) \quad (6)$$

where ρ , \mathbf{u} and e are the density, velocity and specific internal energy of the fluid. P is the pressure that is associated with ρ and E by the equation of state (EOS) Eq. (4). \mathbf{q} represents external heat source, e.g., the electron heat flux in the pellet ablation problem. The current density \mathbf{J} is related to the magnetic field \mathbf{B} through the Ohm's law Eq. (5), in which the electric field is assumed to be curl-free since the magnetic inductance is neglected. The Poisson equation Eq. (6) follows from the local neutrality of weakly ionized plasma.

Across the interface between the ablated plasma and the ambient gas, the pressure and the normal velocity are continuous. At the ablation surface, the ablation rate is determined by the rate of external energy deposition and the latent heat of the ablation.² The electronic boundary condition for the plasma depends on the property of the material at the interface. For dielectric media the normal component of the current in plasma vanishes at the interface, which gives rise to the Neumann boundary condition for the electric potential

$$\frac{\partial \varphi}{\partial \mathbf{n}} = \frac{1}{c} (\mathbf{u} \times \mathbf{B}) \cdot \mathbf{n} \quad (7)$$

where \mathbf{n} is the normal vector at the interface.

2.2. Equation of State and Conductivity Model

Processes of dissociation of diatomic molecules and ionization of atoms in weakly ionized plasmas interacting with external sources such as particle or laser beams are very typical in ablation clouds. These atomic processes

introduce energy sinks and strongly affect plasma temperature and conductivity. In the one temperature, one pressure MHD model, the pressure and specific internal energy of a partially dissociated and partially ionized diatomic gas can be written³ as

$$P = \left(\frac{1}{2} + \frac{1}{2}f_d + f_i \right) \frac{\rho k T}{m} \quad (8)$$

$$e = \left(\frac{1 - f_d}{2(\gamma_m - 1)} + \frac{f_d + f_i}{\gamma - 1} \right) \frac{k T}{m} + \frac{1}{2}f_d \frac{k \epsilon_d}{m} + f_i \frac{k \epsilon_i}{m} \quad (9)$$

where γ_m and $\gamma = 5/3$ are specific heat ratios for molecules and atoms, respectively, k is the Boltzmann constant, m is the mass of the atom (ion). The dissociation $f_d(\rho, T)$ and ionization $f_i(\rho, T)$ fractions are defined as

$$f_d = (n_a + n_i)/n_t$$

$$f_i = n_i/n_t$$

in which $n_t \equiv 2n_g + n_a + n_i = \rho/m$ stands for the total number density of *nuclei*, and n_g , n_a , and n_i denote, respectively, the number densities of gas diatomic molecules, atoms, and ions. The dissociation and ionization fractions can be found from Saha equations¹³ which can be written (in eV units) as^{3,4}

$$\frac{f_i^2}{1 - f_i} = 3.0 \times 10^{21} \frac{T^{\alpha_i}}{n_t} \exp\left(-\frac{\epsilon_i}{T}\right) \quad (10)$$

$$\frac{f_d^2}{1 - f_d} = 1.55 \times 10^{24} \frac{T^{\alpha_d}}{n_t} \exp\left(-\frac{\epsilon_d}{T}\right) \quad (11)$$

where $\alpha_i = 3/2$ and α_d are material dependent parameters. The system of Eqs. (8)–(11) can be used as an EOS closure for a hydrodynamic system of equations written in ρ , \mathbf{u} , T independent variables, as well as for a simple finite difference discretization of such a system. However most of advanced numerical discretization algorithms, including second order MUSCL type schemes and interface propagation algorithms implemented in the FronTier code,¹⁴ are based on solutions of Riemann problems. Solving numerically a Riemann problem requires an ability to calculate the sound speed and integrals of Riemann invariant type expressions along characteristics. For this purpose, we derived the expressions for entropy and other thermodynamic properties of the system (8)–(11) based on the second law of thermodynamics.² To satisfy the requirement of FronTier's hyperbolic solvers and interface propagation routines, we derived the complete set of thermodynamic functions in terms of different pairs of independent variables (ρ, e) , (ρ, P) , (ρ, T) etc. The corresponding algorithms use numerical solvers for complicated nonlinear algebraic equations. The direct use of such algorithms in hydrodynamic simulations was prohibitively expensive. To speedup the code, we created tabulated data of thermodynamic functions and their integrals on a fine mesh in the specific domain of interest before simulations,

and used table look-up and interpolation algorithms during the run.

We use the following model for the electrical conductivity of weakly ionized plasma. Values of the conductivity in the transverse and parallel direction to the magnetic field are the same since the ablation electron collision frequency is much higher than their gyro-frequency.¹⁵ Thus σ is given by the expression^{15,16}

$$\sigma[s^{-1}] = \frac{8.70 \times 10^{13}}{\ln \Lambda \cdot T_e^{-3/2} + 0.054 T_e^{-0.059} (1/f_i - 1)} \quad (12)$$

where f_i is the ionization fraction, T_e is the electron temperature in eV unit, and

$$\Lambda = \frac{1.55 \times 10^{10} T_e^{3/2}}{n_e^{1/2}} \quad (13)$$

where n_e is the electron number density. In the limit $f_i \rightarrow 1$, $\sigma \rightarrow \sigma_{\perp}$, which is the transverse Spitzer conductivity.

3. NUMERICAL ALGORITHM AND IMPLEMENTATION

In this section, we will describe main ideas of numerical methods and their implementation in the FronTier-MHD code for the study of free surface MHD flows at low magnetic Reynolds numbers. More complete description of the algorithm can be found in Ref. [17]. The governing system Eqs. (1)–(7), a coupled hyperbolic–elliptic system in a geometrically complex moving domain, is solved using operator splitting. We use the front tracking hydro code FronTier with free interface support⁹ for solving the hyperbolic subsystem. The Poisson equation for the electric potential can be solved using adaptive techniques for irregular domains described below. The fluid interface is represented as an explicit co-dimension one Lagrangian mesh moving through a volume filling Eulerian mesh. The propagation and redistribution of the interface using the method of front tracking^{8,18} is performed at the beginning of a time step. Then interior states are updated by second order hyperbolic solvers such as the Monotonic Upstream-centered Scheme for Conservation Laws (MUSCL).¹⁹ At the end of the time step, the elliptic system is solved using a finite volume or finite element discretization with interface constraints, and the interior states are updated by adding electromagnetic source terms. The schematic of the algorithm is shown in Figure 1.

Front tracking is an adaptive computational method in which a lower dimensional moving grid is fit to and follows distinguished waves in a flow. Tracked waves explicitly include jumps in the flow state across the waves and keep discontinuities sharp. A key feature is the avoidance of finite differencing across discontinuity fronts and thus the elimination of interfacial numerical diffusion including mass and vorticity diffusion.^{8,18} For free surface MHD

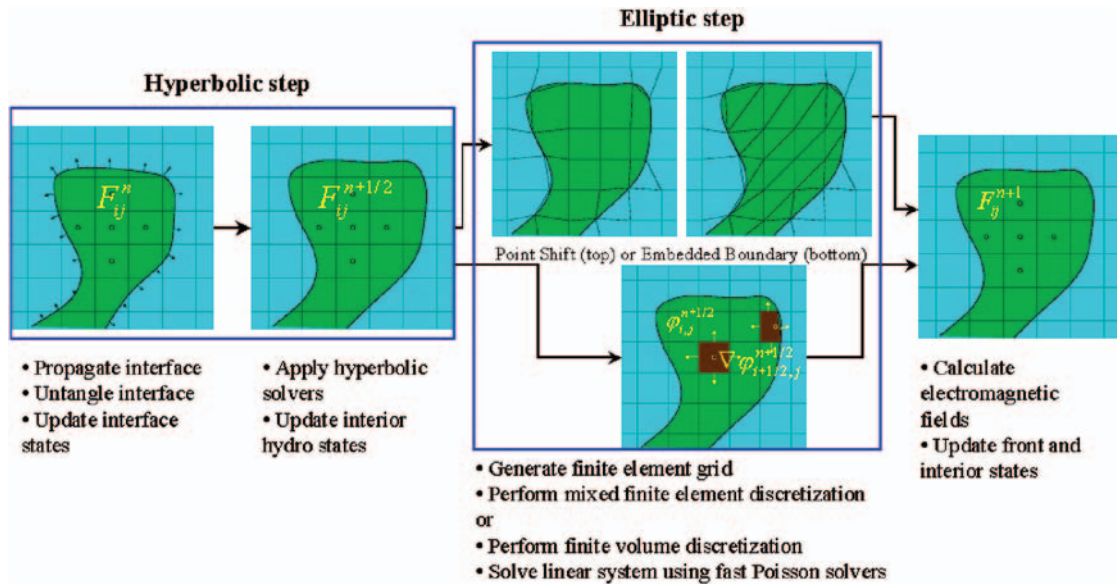


Fig. 1. FronTier-MHD numerical scheme.

flows, we are interested in tracking only fluid interfaces which are contact discontinuity curves of the corresponding Riemann problem²¹ (see Fig. 2). Front tracking is implemented in FronTier,^{9,14} a multiphysics code which is capable of tracking and resolving topological changes of geometrically complex interfaces in two and three space dimensions. Details of the front tracking method and the structure of the FronTier code are described in the above mentioned papers.

The main algorithms implemented in FronTier’s hyperbolic part are as follows.¹⁴ The time step loop starts with the advance of the interface. A computational stencil is constructed at every interface point in the normal and tangential direction, and stencil states are obtained through interpolation. Then Euler equations, projected on the normal and tangential directions, are solved. The normal propagation of an interface point is a predictor-corrector technique. We solve the Riemann problem for left and right interface states to predict the location and states of the interface at the next time step. Then a

corrector technique is employed which accounts for fluid gradients on both sides of the interface. Namely, we trace back characteristics from the predicted new interface location, and then solve Euler equations along characteristics using techniques described in Ref. [14]. After the propagation of the interface points, the new interface is checked for consistency of intersections. The untangling of the interface at this stage consists in removing unphysical intersections, and rebuilding a topologically correct interface.⁹

Two techniques for the redistribution of interfaces and resolving their topological changes, the grid free and grid based tracking, have been developed.⁹ In the first method, interface points are always independent of the rectangular grid while in the second method, the interface points are formed by the intersection of the interface with the rectangular grid lines. Since the first algorithm is more accurate and sufficiently robust, especially in 2D, we use it for the interface propagation in the hyperbolic part of the MHD algorithm. We always transform the interface to the grid based one at the beginning of the elliptic time step since such an interface ideally suits the finite volume discretization technique for the Poisson equation described below. In many practical applications, it is sufficient to solve the elliptic problem once per several hyperbolic time steps.

The final phase of the hyperbolic time step update consists of computing new states on the rectangular spatial grid. Several different shock capturing methods have been implemented in FronTier. They include both directionally split MUSCL¹⁹ type schemes such as the Piecewise Linear, Piecewise Parabolic Method,²² a second order MUSCL scheme developed by Chern, and an unsplit MUSCL scheme.²³ An exact and several approximate Riemann solvers are available for use by these methods.

The existence of a tracked surface, across which physical parameters and the solution change discontinuously,

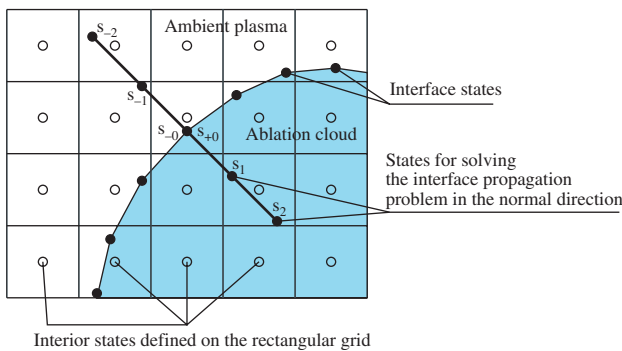
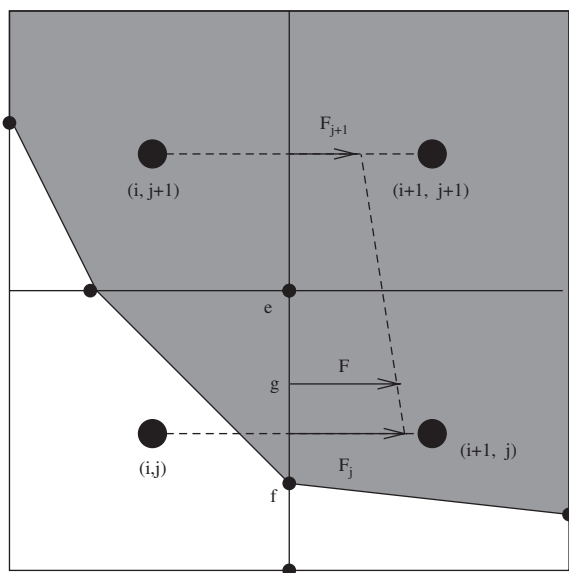
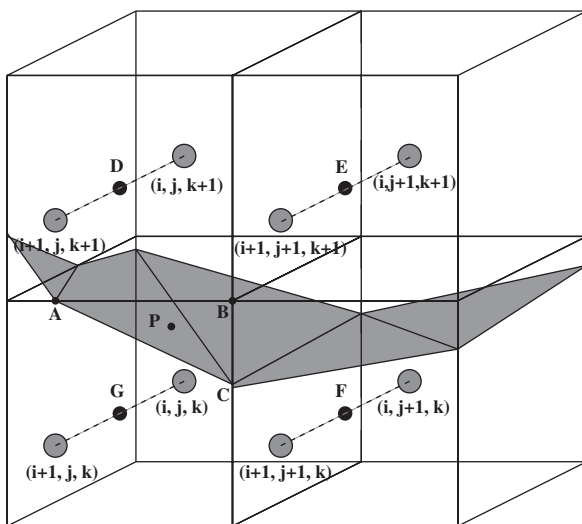


Fig. 2. Rectangular grid, interface, and states for the method of front tracking. States contain density, momentum, and energy density of the fluid (plasma), and references to the EOS model and other parameters.

has important implications for the solution of an elliptic or parabolic system. We have developed an algorithm and software for the dynamic generation of finite element meshes conforming to the interface based on the point shift technique. In this method, we shift rectangular grid points to the interface as shown by the top row images of the elliptic step in Figure 1. In this process, the grid conforms to the interface while it remains logically rectangular. Then it is split into triangular (2D) or tetrahedral (3D) finite elements, and a mixed finite element discretization using Whitney elements in 3D²⁴ or Raviart-Thomas elements in 2D is performed. The corresponding parallel linear equation solver uses non-overlapping domain decomposition and a parallel wire-basket technique.²⁵



(a) Linear flux interpolation in 2D



(b) Bi-linear flux interpolation in 3D

Fig. 3. Schematic of the linear and bi-linear flux interpolation.

The finite element solver based on point shift grids dynamically conforming to the moving interface has not been sufficiently robust for complex 3D interfaces. To improve the ability of the code to handle complex 3D domains, we have implemented an elliptic solver based on the embedded boundary method.^{10,20} The embedded boundary method is based on the finite volume discretization in grid blocks defined by the rectangular Cartesian grid and the interface. The solution is treated as a regular block centered quantity, even when these centers are outside of the domain. However the source terms and the right hand side are interpolated in geometrical centers (centroids) of partial grid blocks and their facets, respectively, cut by the interface (Fig. 3). This treatment has the advantages of dealing with geometrically complex domains and ensures second-order accuracy of the solution. For the accuracy of the algorithm and the stability near the interface, the calculation of fluxes across cut sells is done using linear (2D) and bi-linear (3D) interpolation of fluxes in the neighboring cells, as illustrated in Figure 3. We use parallel iterative solvers implemented in the PETSc²⁶ and HYPRE²⁷ packages for solving the corresponding linear systems.

4. APPLICATIONS

4.1. Pellet Ablation in Tokamaks

The injection of frozen pellets of deuterium and tritium is considered the major mechanism for fueling of nuclear fusion reactors of the tokamak configuration. This problem is significantly important for International Thermonuclear Experimental Reactor (ITER).²⁸ The ablation of tokamak pellets has been studied using several semi-analytical^{4, 15, 29, 30, 32} and numerical^{3, 33} approaches. In this section, we illustrate the use of the MHD algorithm with a summary of our studies of the pellet ablation in tokamaks. More details are given in Ref. [2].

The schematic of the pellet ablation problem is shown in Figure 4. The frozen deuterium-tritium pellet of radius 2 mm is shot into a tokamak plasma ($T_e = 2$ keV, $n_e = 10^{14}$ cm⁻³). In the simulations the pellet is initialized with a thin covering of ablation cloud surrounded by the ambient plasma. Almost unattenuated hot electrons streaming in both directions along the z axis hit the pellet and cause the rapid ablation. As the pellet moves across the plasma pedestal, the plasma around the pellet gradually becomes hotter and denser. The time it takes for the heat flux to ramp up is called the warm-up time. It is equal to the plasma pedestal width divided by the pellet velocity. In the code, the warm-up process is numerically implemented as a linear increase of the heat flux of hot plasma electrons from zero to its maximum value during the warm-up time. The ablation cloud effectively shields the pellet from incoming electrons by absorbing most of their energy. As the temperature of the ablated gas increases the

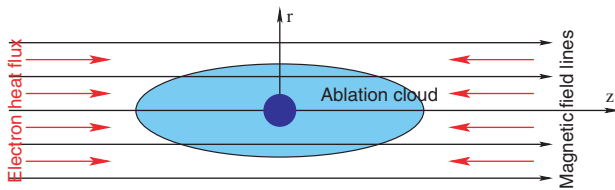


Fig. 4. Schematic of the hydrogen pellet in a tokamak.

dissociation and then ionization processes take place causing nonlinear waves in the cloud, and the created weakly ionized plasma flows along the magnetic field lines.

We assume the axial symmetry of the problem, and solve equations in the cylindrical axisymmetric coordinate system r, z . However, the actual shape of the ablation channel in a real tokamak magnetic field ($\nabla \mathbf{B}$ induced bending of the channel) can be studied only in 3D. The assumption of a perfectly axisymmetric channel in an unbounded domain would lead to a steady increase in the shielding of the pellet, causing the ablation rate to approach zero asymptotically in time. To eliminate these unphysical consequences, we used estimates of Ref. [31] to obtain the effective shielding length of 15 cm. Numerically, we limited the interaction of the ablation channel with the plasma heat flux to the shielding length, and applied the outflow boundary conditions in both r - and z -direction to minimize reflection of waves.

Realistic EOS are employed in different geometrical regions corresponding to different states of matter.³ In particular, atomic physics processes in the ablation cloud such as dissociation and ionization are taken into account by the plasma EOS described by Eqs. (8) and (9). A surface ablation model is used at the pellet surface to model the solid-vapor transition phase change.² A kinetic-based electron heat flux model for the calculation of the thermal energy deposition ($-\nabla \cdot \mathbf{q}$ in Eq. (3)) in the ablation cloud and on the pellet surface uses the analytical model of Refs. [3, 34].

An inherent limitation of all previous ablation models has been the absence a self-consistent and rigorous inclusion of the interaction of the ionized ablation flow with the magnetic field. Near the pellet, the ablation is highly resistive, and thus the pressure gradient force largely balances the inertial force resulting in a nearly isotropic flow pattern. Farther downstream, the Lorentz force eventually overwhelms the inertial force, and tends to funnel the flow along the magnetic field lines, forming a long, narrow ablation channel. The question of whether the ablation channel would offer the pellet additional shielding from the incident parallel electron heat flux has remained an open question for a long time. The main motivation for this study was to incorporate these MHD effects, the Lorentz force and the attendant Joule heating.

We validated² the developed model by comparison with analytical predictions²⁹ and previous numerical simulations³ of pure hydrodynamic models (no MHD forces), and used it to study the pellet ablation physics,

i.e., the structure of the ablation flow and pellet ablation rates in magnetic fields. In the presence of a magnetic field, the ionization of the pellet ablation cloud by the electron heat flux leads to the channeling of the ablation flow along magnetic field lines. We found that this effect is sensitive to the warm-up time. Longer warm-up time leads to a slower increase of temperature and wider ablation flow channels.

In addition to the formation of the ablation channel, the action of the magnetic field completely changed the structure of the ablation flow. The distributions of Mach number are depicted in Figure 5. The double transonic flow structure, similar to the one predicted by the hydrodynamic model,³ remained in the ablation channel at $t = 3 \mu\text{s}$ (Fig. 5(a)). However at $t = 9 \mu\text{s}$, the entire flow in the ablation channel was transformed into subsonic (Fig. 5(b)).

At a finite shielding length (15 cm in our simulations) the ablation flow converged into steady state. The Mach number, temperature and pressure along radial direction and the longitudinal direction in the steady-state flow are shown in Figure 6. These simulations were performed at $10 \mu\text{s}$ warm-up time. The steady state flow was subsonic everywhere in the channel, with the Mach number reaching 1 at the exit. The pressure slowly decreased towards the channel exit, while the temperature increased with the longitudinal coordinate. The nonlinear behavior of the temperature and Mach number near the pellet surface was caused by the atomic processes in the ablation cloud.

Calculated values of the ablation channel width and ablation rate are listed in Table I. As expected, both the channel width and the ablation rate reduce with the increase of magnetic field. Compared to the ablation rate with MHD effect neglected, 54 g/s, the magnetic field reduced the ablation rate to 44%, 37%, 33% in the 2, 4, 6 Tesla fields respectively. Therefore, we concluded that the magnetic field can significantly reduces the ablation

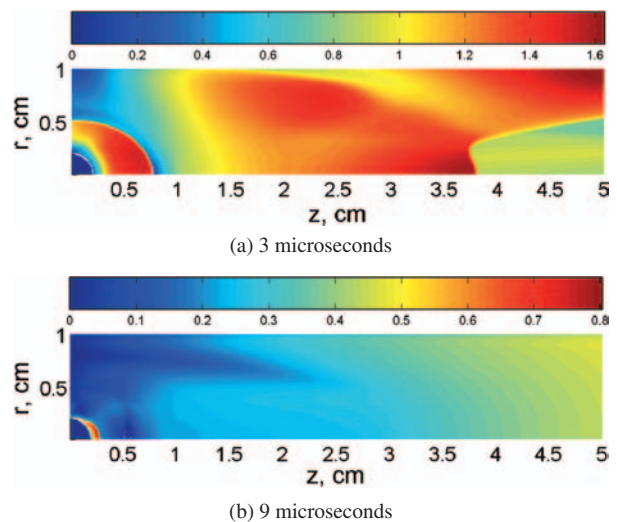


Fig. 5. Mach number distribution in the ablation flow near the pellet in 6 Tesla magnetic field with warm-up time $20 \mu\text{s}$.

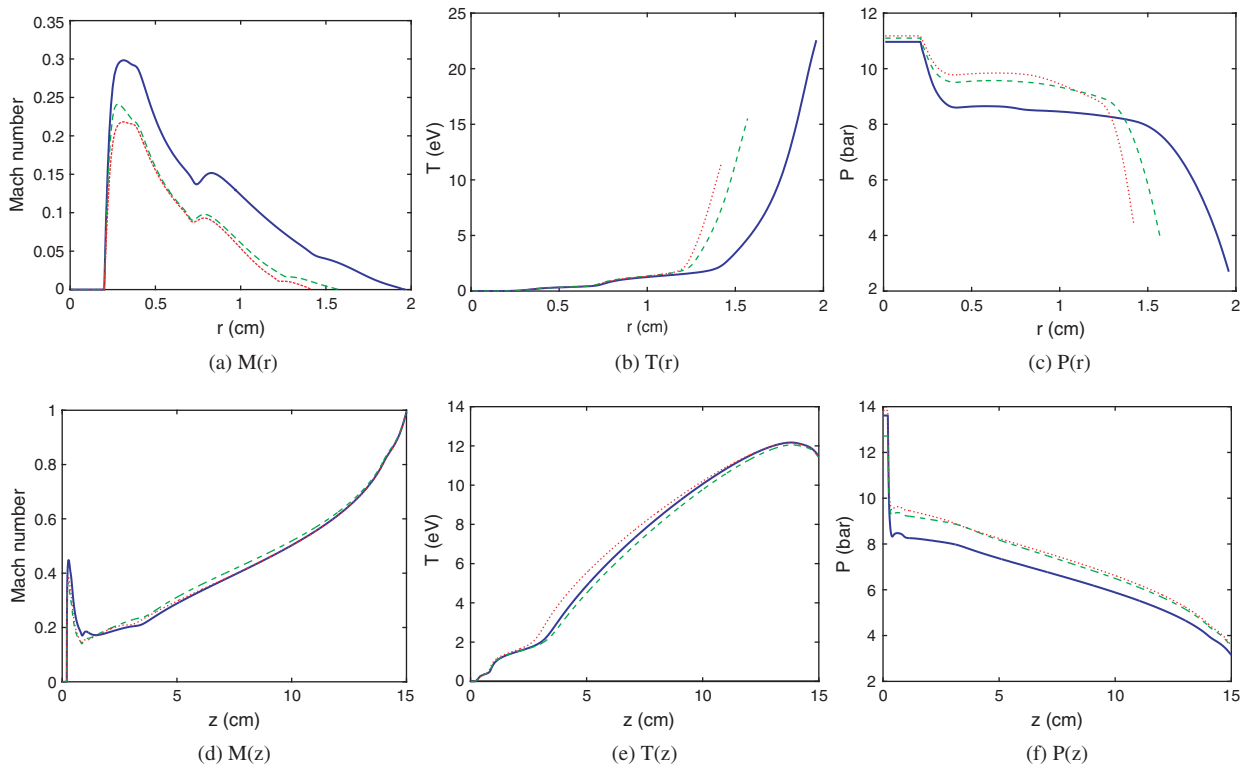


Fig. 6. Steady-state mach number, temperature and pressure distributions along the r -axis and the z -axis. Warm-up time is $10 \mu\text{s}$. Solid line: $B = 2$ Tesla, dashed line: $B = 4$ Tesla, dotted line: $B = 6$ Tesla.

rate due to the increased shielding of the pellet by long ablation channels, provided that the warm-up time is small, as is expected for ITER.²

In order to justify the low magnetic Reynolds number approximation of the MHD equations, we calculated the near-field and far-field inductance rate $|\Delta B/B|$. The induced magnetic field near the pellet was calculated using the Biot-Savart law. Far from the pellet along the channel, the inertial term in momentum equation is considered to be small, and $|\Delta B/B|$ is half the magnetic $\beta = 8\pi P/B^2$, which is the ratio of the channel kinetic pressure to the magnetic field pressure. It has been found out that so long as the electrostatic reduction of the electron heat flux is taken into account, the inductance rate is of the order of 0.1 or lower. Therefore, we conclude that Faraday's law is indeed negligible for realistic tokamak parameters.

4.2. Laser Ablation Plasma Plume

Magnetic fields are used for the control of the dynamic properties of transient plasmas induced by laser ablation.¹

Table I. Channel radius and ablation rate in various magnetic fields. The warm-up time is $10 \mu\text{s}$.

Magnetic field (Tesla)	2	4	6
Channel radius (cm)	1.96	1.57	1.42
Ablation rate (g/s)	24	20	18

The laser ablation in magnetic fields was studied experimentally in Ref. [1] as a method of diverting or extracting energy from the highly ionized expanding plasma generated in inertial confinement fusion (ICF) target explosions. The plasma conductivity in ICF target explosions is very large and the ablation process is beyond the applicability of low magnetic Reynolds number approximation,¹ at least at its initial stage. The plasma created in the process of nanotube synthesis is usually weakly ionized and the induced magnetic field is usually much smaller than the applied field. We simulated the expansion of laser-generated plumes using the FrontTier code equipped with the elliptic solver and the EOS for partially ionized gas. The laser and material settings are similar to those in Labão and Povitsky's papers.^{35,36} We investigated the MHD effect and observed changes in plume structure and dynamics in the presence of the magnetic field.

In our computational model, the interface between the ablated plasma plume and the cold nonconducting ambient gas is tracked explicitly (see Fig. 7). In the presence of magnetic fields, the Poisson problem Eqs. (6) and (7) is solved in the plasma region. For cases of zero magnetic field (Fig. 7(a)) or longitudinal magnetic fields (Fig. 7(b)), the plume expansion is axially symmetric. In transverse magnetic fields (Fig. 7(c)) plumes become wedge-shaped and must be simulated in 3D.

The interaction of the laser beam with the evaporating material leads to the formation of an isothermally

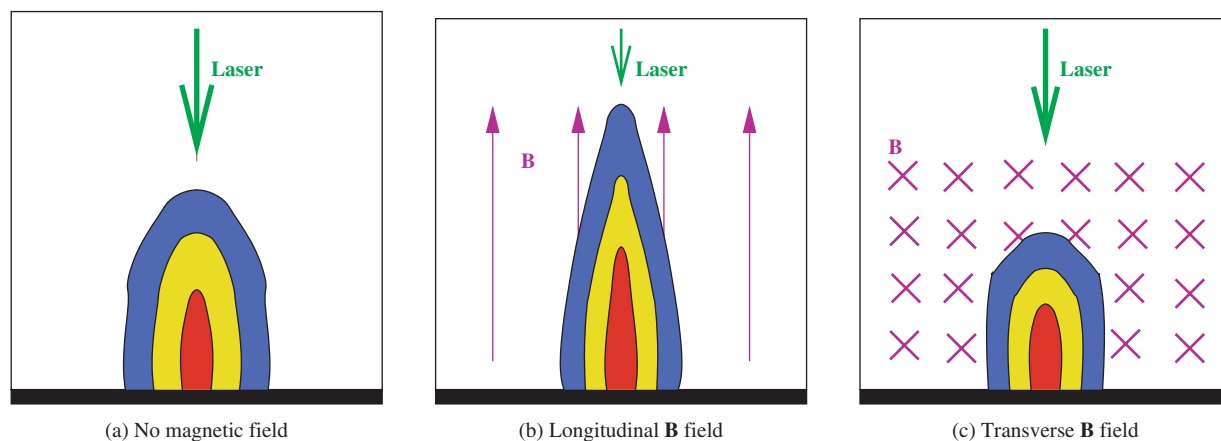


Fig. 7. Schematic of the expansion of laser induced plasma plumes.

expanding plasma and this persists until the end of the laser pulse; after the termination of the laser pulse, no particles are ejected from the target surface.³⁷ Our simulations were started from either the beginning or the end of the laser pulse. In the first approach, the laser beam ablates the solid target and brings energy along with mass into the plasma plume, and the ablated material expands during the time of the laser pulse. After the termination of the pulse, the target surface is treated as a reflecting boundary. In the second approach, a thin layer near the target is initialized as the hot ablated material, and the target surface is always taken to be a reflecting boundary. Since the simulated plume expansion time (several microseconds) is much longer than the laser pulse duration (20 nanoseconds), both approaches gave essentially the same results.

In the simulations presented here, the container is initially filled with the argon gas at temperature 1500 K (0.13 eV) and pressure 0.01 bar. A laser beam of 2 mm diameter is focused on the surface of a carbon target, creating the ablated vapor with the initial pressure of 100 bar and temperature of 5 eV. Since the ionization energy of carbon is 11.26 eV, the carbon vapor is weakly ionized.

The injection velocity of the ablated material is set to zero. After the end of the laser pulse, the carbon surface is treated as a fixed wall (normal velocity of vapor on the wall is zero). Flow through condition is applied to all other boundaries of the computational domain to represent a large container that does not interfere with the expansion of the plasma plume.

First we studied the evolution of the plume front in longitudinal magnetic fields. Both two dimensional axisymmetric and three dimensional simulations were carried out. The grid resolution used in the simulations was 0.02 cm, and the grid size for a typical 3D simulation is $200 \times 200 \times 100$. The 2D and 3D simulation results agree within a few percent. For example, in a 2 Tesla magnetic field, 2D simulation showed that the plume grew to the height of 0.73 cm and radius (at base) of 0.36 cm after 1 microsecond; while 3D simulation predicted the height of 0.76 cm and radius of 0.34 cm. We verified that the deviation is mainly attributed to the treatment of geometrical source terms introduced by cylindrical coordinates in 2D simulations. The 3D plume fronts in longitudinal magnetic fields are shown in Figure 8. Figure 9 shows the evolution of the plume front in longitudinal magnetic fields. In the

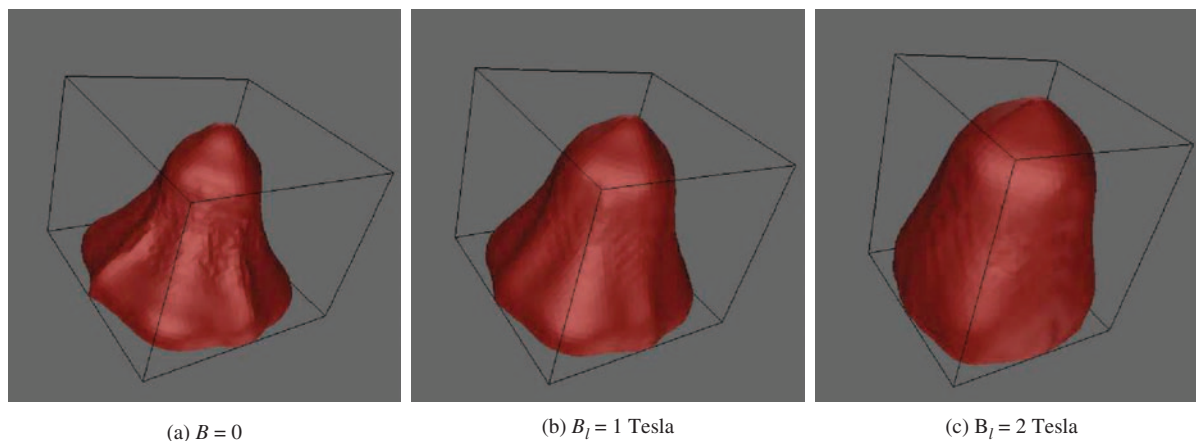


Fig. 8. Three dimensional plume fronts at $t = 1 \mu\text{s}$ in longitudinal magnetic fields.

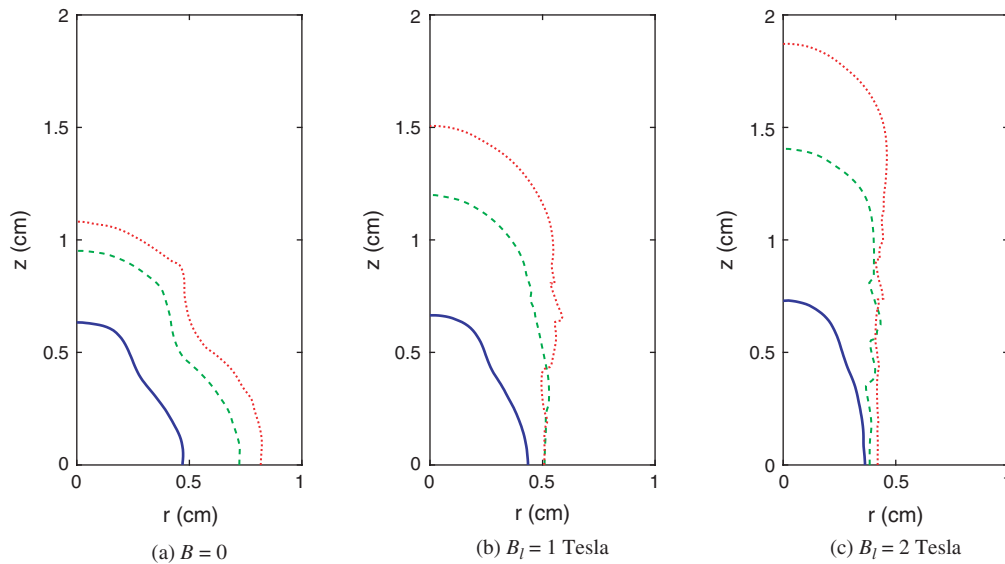


Fig. 9. Evolution of the plume front in longitudinal magnetic fields. In each figure, the solid curve is for $t = 1 \mu\text{s}$, the dashed curve is for $t = 5 \mu\text{s}$, the dotted curve is for $t = 10 \mu\text{s}$.

absence of the magnetic field, the plume front is close to spherical as shown in Figure 9(a). In magnetic fields, the plume is channeled along the field lines and the longitudinal expansion is boosted while the transverse expansion is suppressed, as shown in Figures 9(b and c).

Figure 10 shows the MHD effect of longitudinal magnetic fields on the plume evolution quantitatively. It is clear from the figure that the spherical expansion in the absence of the magnetic field slows down quickly with increasing time. But in magnetic fields the expansion is almost one-dimensional – there is no significant slowing down of the longitudinal expansion, while the transverse expansion almost completely stops. The peak values of longitudinal and transverse expansion velocities at $t = 10 \mu\text{s}$ in the absence of the magnetic field are 419 m/s and 439 m/s respectively. In the 2 Tesla field the corresponding values are 1310 m/s and 25 m/s. Besides the change of the plasma plume velocity distribution in the magnetic field, the plasma density and pressure significantly increase. For example, the peak value of the plume density at $10 \mu\text{s}$ increases from $1.0 \times 10^{-7} \text{ g/cm}^3$ in the absence of the magnetic field to $2.0 \times 10^{-7} \text{ g/cm}^3$ in the 2 Tesla field, while the maximum pressure increases from 9 mbar to 19 mbar.

We also studied the effect of transverse magnetic fields on the plasma plume expansion. Due to the loss of axisymmetry, only three dimensional simulations are applicable. The plasma plumes in 1 and 2 Tesla transverse magnetic fields are plotted in the Figure 11. It shows that with the increase of the magnetic field, the plume expansion is extended in one direction (parallel to field lines) and reduced in other directions (perpendicular to the field lines).

Assuming the magnetic field along y-axis, we also plotted the contours of the density distribution in the cross

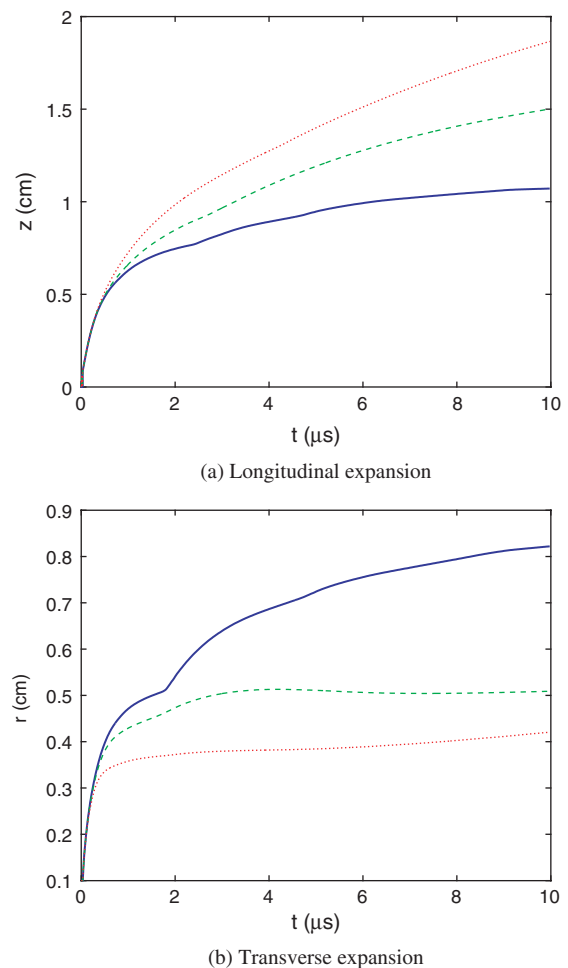


Fig. 10. Longitudinal and transverse expansion of the plume in the longitudinal magnetic fields. In each figure, the solid curve is for $B = 0$, the dashed curve is for $B = 1 \text{ Tesla}$, the dotted curve is for $B = 2 \text{ Tesla}$.

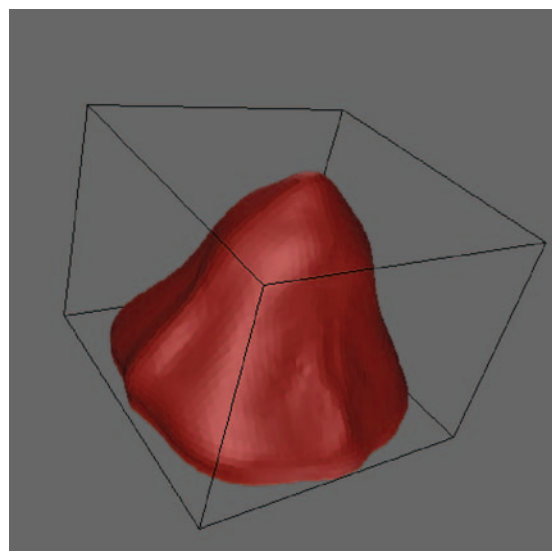
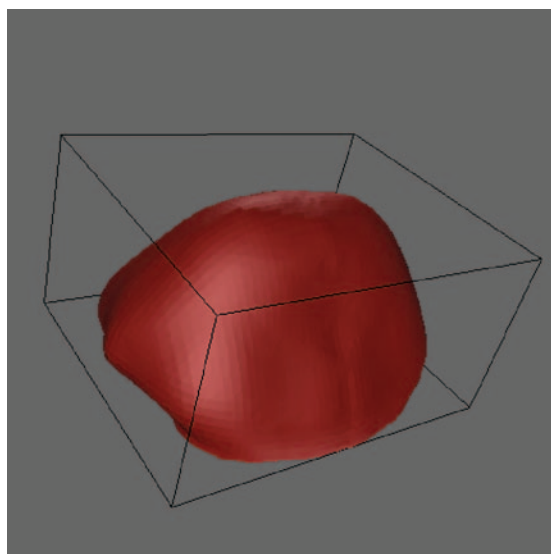
(a) $B_t = 1$ Tesla(a) $B_t = 2$ Tesla

Fig. 11. Three dimensional plume fronts at $t = 1 \mu s$ in transverse magnetic fields.

sections of the plume in xz and yz planes respectively in Figure 12. In the plane perpendicular to the magnetic field, the plume density is higher in the center as expected. In the plane parallel it is found that the plume density is approximately uniform along the field lines. The dark regions in the bottom of the plume stand for the nearly vacuum region created by the fast expansion of plasma plume. The zigzag boundary of the plume comes from the interpolation used in the calculation of contours, the actual tracked interface is a smoother triangulated two dimensional manifold.

From the MHD simulations of plasma plume expansion, we conclude that the magnetic field is an effective tool to enhance, control, or direct the expansion. Finally, to

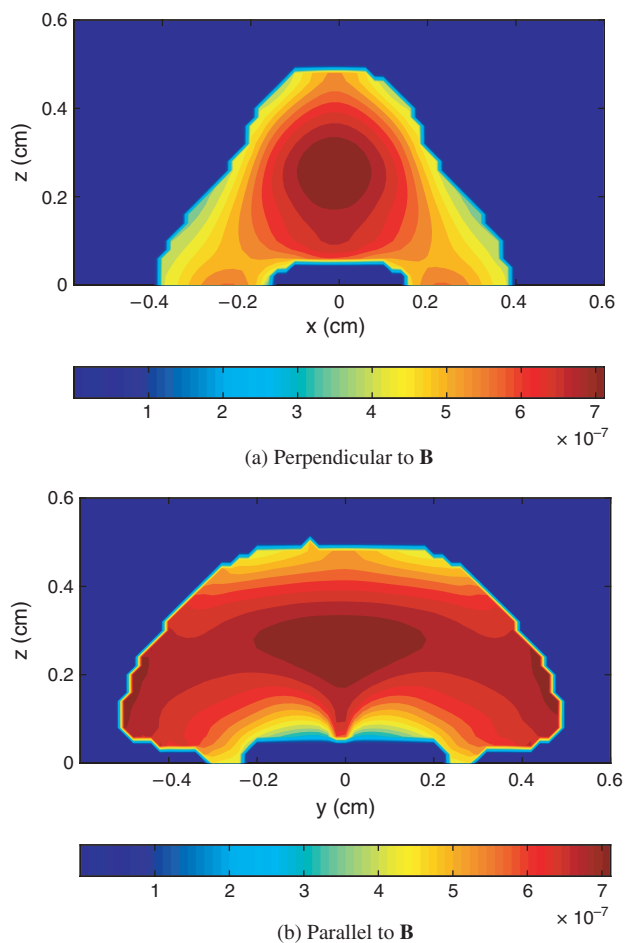


Fig. 12. Density distribution in the cross sections of the plasma plume in 2 Tesla transverse magnetic fields. $t = 1 \mu s$. The unit of the density is g/cm^3 .

justify the low magnetic Reynolds number approximation, we calculated the induced magnetic field ΔB at the center of the plume using Biot-Savart law. Indeed we found that $\Delta B/B \ll 1$ in our simulations. For the longitudinal magnetic field, the ratio $\Delta B/B$ attains maximum at about 90 nanoseconds after the end of the laser pulse, and in both 1 Tesla and 2 Tesla fields the maximum value of $\Delta B/B$ is only 0.002.

5. CONCLUSIONS

We have described a numerical algorithm for the simulation of free surface magnetohydrodynamic flows of ablated material at low magnetic Reynolds numbers. The corresponding governing equations constitute a coupled hyperbolic–elliptic system in a geometrically complex and evolving domain. The numerical algorithm includes the interface tracking technique for the hyperbolic problem, a Riemann problem for the material interface, discretization of elliptic equations in irregular domains with interface constraints using the embedded boundary method, and

high performance parallel solvers such as MUSCL-type schemes for hyperbolic problems and iterative solvers implemented in the PETSc and HYPRE packages. An extensive theoretical analysis of the method of front tracking for hyperbolic systems of conservation laws has already been performed earlier works, and the method has been validated and tested on problems of Rayleigh-Taylor and Richtmyer-Meshkov surface instabilities. The elliptic technique was validated in Ref. [17] and shown to be second order accurate for both the electric potential and its gradient. A numerical model for the equation of state accounting for atomic processes in weakly ionized plasmas has been developed. The numerical algorithms are applicable to free surface MHD flows of conducting liquids and weakly ionized gases interacting with external energy sources.

The use of the algorithm in 2D has been illustrated by the study of the ablation of injected deuterium pellets in tokamaks. We have shown that the increase of the magnetic field reduces the ablation channel width and the pellet ablation rate significantly. This process is sensitive to the value of the parameter “warm-up time,” and longer warm-up times increase both the ablation channel width and ablation rate. The directional channeling of the ablated material leads to the redistribution of density and a much stronger shielding in the channel far from the pellet compared to the spherically symmetric case. In the future, full 3D simulations of pellet ablation will be carried out for the study of striation instabilities.

In this work, MHD algorithm was applied to the simulation of the expansion of laser-generated plasma plumes in magnetic fields. Both longitudinal and transverse magnetic fields have been studied. We confirmed quantitatively that the longitudinal magnetic field would channel the plasma plume. Although the maximum temperature of the plume is less than half of the ionization energy, the spherical expansion is changed to one-dimensional expansion in 1 Tesla field, and the longitudinal expansion is significantly enhanced while the transverse expansion is completely stopped in a few microseconds. In the transverse magnetic field, the plume expansion is directed along the magnetic field lines, and the expansion in other directions is reduced. Therefore our MHD simulations confirms the effectiveness of magnetic fields as a method to control the ablation flow, and provides a way to test physical settings without going through expensive experiments.

In the future, the full MHD system will be coupled to the front tracking method and the *FronTier* code. This will enable the simulation of highly conducting ablation flows for which the low magnetic Reynolds number approximation does not apply.

Acknowledgments: The authors would like to thank Paul Parks for his guidance on the pellet ablation physics and stimulating discussions. This manuscript has been

authored in part by Brookhaven Science Associates, LLC, under Contract No. DE-AC02-98CH10886 with the U.S. Department of Energy. The United States Government retains, and the publisher, by accepting the article for publication, acknowledges, a world-wide license to publish or reproduce the published form of this manuscript, or allow others to do so, for the United States Government purpose. This research partially used resources of the National Energy Research Scientific Computing Center, which is supported by the Office of Science of the U.S. Department of Energy under Contract No. DE-AC03-76SF00098.

References and Notes

1. S. S. Harilal, C. V. Bindhu, and M. S. Tillack, *Phys. Rev. E* 69, 026413 (2004).
2. R. Samulyak, T. Lu, and P. Parks, *Nucl. Fusion* 47, 103 (2007).
3. R. Ishizaki, P. B. Parks, N. Nakajima, and M. Okamoto, *Phys. Plasmas* 11, 4064 (2004).
4. F. S. Felber, P. B. Parks, R. Prater, and D. Vlasow, *Nucl. Fusion* 19, 1061 (1979).
5. J. L. Delcroix, *Weakly Ionized Gases, Plasma Physics*, Wiley (1965) Vol. 1–2.
6. N. Morley, S. Smolentsev, R. Munipalli, M.-J. Ni, D. Gao, and M. Abdou, *Fusion Eng. Design* 72, 3 (2004).
7. J. W. Davis and G. L. Kulcinski, *Nucl. Fusion* 16, 355 (1976).
8. J. Glimm, J. Grove, X. L. Li, K. L. Shyue, Q. Zhang, and Y. Zeng, *SIAM J. Sci. Comp.* 19, 703 (1998).
9. J. Glimm, J. Grove, X. L. Li, and D. C. Tan, *SIAM J. Sci. Comp.* 21, 2240 (2000).
10. H. Johansen and P. Colella, *J. Comput. Phys.* 147, 60 (1998).
11. S. Oshima, R. Yamane, Y. Moshimaru, and T. Matsuoka, *JSME Int. J.* 30, 437 (1987).
12. S. Molokov and C. B. Reed, Review of free-surface MHD experiments and modeling, Technical Report ANL/TD/TM99-08, Argonne National Laboratory (1999).
13. Y. B. Zel’dovich and Y. P. Raizer, *Physics of Shock Waves and High-Temperature Hydrodynamic Phenomena*, Academic, New York (1966), Vol. I.
14. J. Glimm, J. Grove, and Y. Zhang, *SIAM J. Sci. Comp.* 24, 208 (2002).
15. P. Parks, *Nucl. Fusion* 20, 311 (1980).
16. I. P. Shkarofsky, T. W. Johnston, and M. P. Bachynski, *The Particle Kinetics of Plasmas*, Addison-Wesley Publishing Co. (1966).
17. R. Samulyak, J. Du, J. Glimm, and Z. Xu, *J. Comp. Phys.* (2007), Submitted.
18. I. R. Chern, J. Glimm, O. McBryan, B. Plohr, and S. Yaniv, *J. Comput. Phys.* 62, 83 (1986).
19. B. van Leer, *J. Comput. Phys.* 32, 101 (1979).
20. P. Schwartz, M. Barad, P. Colella, and T. Ligocki, *J. Com. Phys.* 211, 531 (2006).
21. R. Courant and K. Friedrichs, *Supersonic Flows and Shock Waves*, Interscience, New York (1948).
22. P. Colella and P. Woodward, *J. Comput. Phys.* 54, 174 (1984).
23. P. Colella, *J. Comput. Phys.* 87, 171 (1990).
24. H. Whitney, *Geometric Integration Theory*, Princeton University Press, Princeton (1957).
25. L. C. Cowsar, J. Mandel, and M. F. Wheeler, *Math. Comput.* 64, 989 (1995).
26. S. Balay, W. Gropp, L. McInnes, and B. Smith, *PETSc Users Manual*, ANL-95/11-Revision 2.1.1, Argonne National Laboratory (2001).
27. Hype: High performance preconditioners, <http://www.llnl.gov/CASC/hype>

28. F. W. Perkins, D. E. Post, N. A. Uckan, and et al., *Nucl. Fusion* 39, 2391 (1999).
29. P. Parks and R. Turnbull, *Phys. Fluids* 21, 1735 (1978).
30. B. V. Kuteev, et al., *Sov. J. Plasma Phys.* 11, 236 (1985).
31. P. B. Parks, *Nucl. Fusion* 32, 2137 (1992).
32. P. B. Parks and M. N. Rosenbluth, *Phys. Plasmas* 5, 1380 (1998).
33. A. K. MacAulay, *Nucl. Fusion* 34, 43 (1994).
34. P. B. Parks, W. D. Sessions, and L. R. Baylor, *Phys. Plasmas* 5, 1968 (2000).
35. D. C. Lobão and A. Povitsky, *Lecture Notes in Computer Science* 2668, 871 (2003).
36. D. C. Lobão and A. Povitsky, *AIAA Journal* 43, 595 (2005).
37. S. S. Harilal, C. V. Bindhu, M. S. Tillack, F. Najmabadi, and A. C. Gaeris, *J. Appl. Phys.* 93, 2380 (2003).

Received: xx Xxxx xxxx. Revised/Accepted: xx Xxxx xxxx.